Article

Electron Spin Relaxation Studies of Polydopamine Radicals

Krzysztof Tadyszak,* Radosław Mrówczyński, and Raanan Carmieli

ACCESS | 📊 Metrics & More | 📰 Article Recommendations

ABSTRACT: We present a thoroughgoing electron paramagnetic resonance investigation of polydopamine (PDA) radicals using multiple electron paramagnetic resonance techniques at the W-band (94 GHz), electron nuclear double resonance at the Q-band (34 GHz), spin relaxation, and continuous wave measurements at the X-band (9 GHz). The analysis proves the existence of two distinct paramagnetic species in the PDA structure. One of the two radical species is characterized by a long spin–lattice T_1 relaxation time equal to 46.9 ms at 5 K and is assigned to the radical center on oxygen. The obtained data revealed that the paramagnetic species exhibit different electron spin relaxation behaviors due to different couplings to local phonons, which confirm spatial distancing between two radical types. Our results shed new light on the radical structure of PDA, which is of great importance in the application of PDA in materials science and biomedicine and allows us to better understand the properties of these materials and predict their future applications.
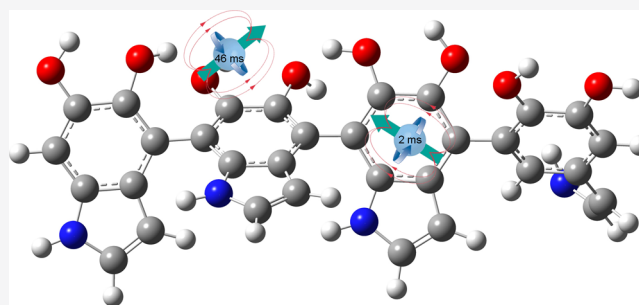
INTRODUCTION

Melanins are naturally occurring compounds, usually identified as responsible for pigmentation in living organisms, and can be found in *Calliphora puparia*, sepia inks, and human hairs as a product of L-dopa oxidation. Because of the large similarity of structural and electronic features between melanins and polydopamine (PDA), the latter is often called artificial melanin. This new material shows a variety of desired attributes, that is, it is nontoxic and biocompatible, can bind metal ions, and possesses strong photothermal properties. Moreover, PDA is obtained via simple and cheap oxidative polymerization of dopamine under basic conditions; thus, PDA has drawn scientific attention for multiple applications. So far, it has been applied in the preparation of antibacterial materials[1] as a platform for tissue engineering[2] for the preparation of artificial photosynthesis.[3] It was also used in tailoring organocatalytic[4] and photocatalytic properties[5,6] of coated materials and the synthesis of multifunctional drug delivery systems.[7–10] Furthermore, the reactivity toward molecules bearing amino moieties made PDA-coated supports suitable for the immobilization of enzymes[11,12] and a variety of biomolecules.[13] PDA exhibits strong adhesive properties toward myriad materials, that is, Teflon, wood, stainless steel, polylactic acid, silica, iron oxides, aluminum oxide, noble metals (Au, Ag, Pt, and Pd),[14–17] and iron oxides.[9,18–23] It is also a chelating agent capable of the reversible complexation of a majority of transition metals.

In 1960, it was stated by Longuet-Higgins[24] that melanin is a conjugated chain of quinonoid units, which could be called a quinone-semiquinone copolymer. Nevertheless, even after many years, the structure of melanin and PDA is still elusive.[25–27] One of the recently proposed models assumed that PDA is not a covalent polymer but instead a supramolecular aggregate of monomers, which are noncovalently bonded, held together by strong, noncovalent forces, including charge transfer, π-stacking, and hydrogen bonding.[27] The results obtained from UV–visible (UV–vis), crystallographic studies and DFT calculation suggest a chemically disordered structure of melanin.[28] The electronic structure of PDA resembles a semiconductor due to electron and hole-type conductivity possible after the attaching/detaching of protons.

In this article, we will shed light on the radical structure of PDA using continuous wave (CW-EPR) and pulse electron paramagnetic resonance (pulse-EPR) techniques at different frequencies. We demonstrate that at least two radical species exist in PDA. One is carbon, and the second is the oxygen-centered semiquinone radical.[29–32] Both of them can be distinguished using pulse EPR methods, especially by an electron spin relaxation study.
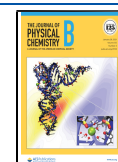
EXPERIMENTAL SECTION

Chemicals. Dopamine hydrochloride and tris-(hydroxymethyl)aminomethane (Tris) were purchased from
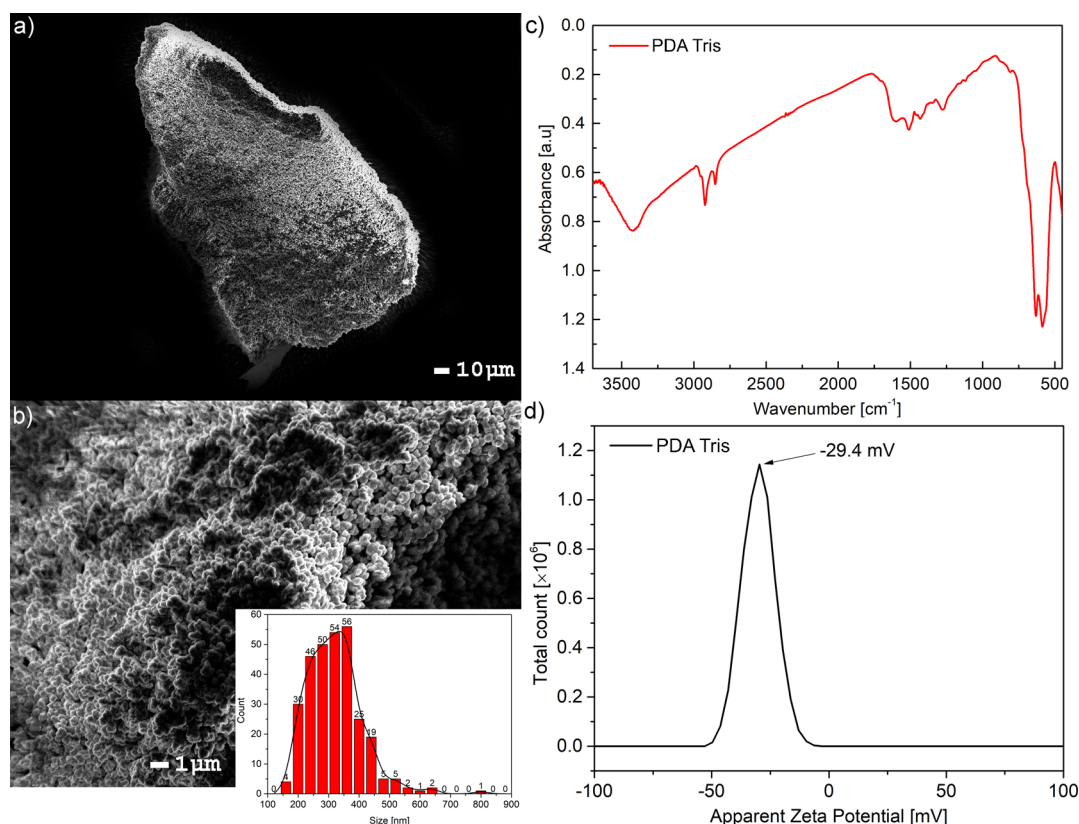
Figure 1. (a) PDA micrograph, with a scale of 10 μm; (b) PDA micrograph, with a scale of 1 μm; (inset) nanoparticle size distribution; (c) FTIR spectrum of PDA from Tris; (d) zeta potential of PDA in water.

Alfa Aesar and used without any purification. In all steps, Milli-Q deionized water (resistivity 18 MΩ·cm) was used.

Polydopamine Preparation. Dopamine hydrochloride (1 g, 5.3 mM) was dissolved in 500 mL of 10 mM buffer (Tris pH = 8.5 and phosphate pH = 8.5) and stirred under air for 24 h. The resulting black precipitate was separated by centrifugation (400 rpm, 15 min), washed with water (100 mL), and centrifuged again. This washing step was repeated three times, and the solid was dried at 50 °C overnight. The sample was measured in an ambient atmosphere after 2 months after preparing. The number of spins was obtained at the X-band using the experimental, simultaneous comparative method. As a standard, monocrystals of copper sulphate pentahydrate were used. The amount of moisture was deduced by the change of weight before and after drying for 48 h at 70 °C.

Fourier Transform Infrared Spectroscopy. The Fourier transform infrared (FTIR) spectrum was recorded with a Bruker TENSOR 27 spectrometer. PDA was mixed with KBr and used as pallets.

Zeta Potential. The zeta potential was measured with a Malver Zetasizer Nano ZS after preparing the PDA suspension in water.

Scanning Electron Microscopy. Scanning electron microscopy (SEM) studies were performed with a 7001TTLS microscope JEOL with a 10 kV accelerating voltage without any metal coating. Particle size statistics was done with ImageJ software manually.

Electron Paramagnetic Resonance Spectroscopy. The spectroscopic CW-EPR measurements were performed with a RADIOPAN SX spectrometer equipped with an Oxford CF935 cryostat, which allowed measurements in the temper-

ature range of 4.2−300 K. The modulation amplitude was 0.05 mT, the microwave power was 11.38 mW (line without saturation effects), and the microwave frequency was recalculated for each measured point to exactly 9 GHz. The number of points per spectra was 1024, the accumulation was 2, and the time per one point was 120 ms (4.2 K) to 520 ms (300 K).

The EPR relaxation measurements were conducted with an ELEXSYS E580 EPR Spectrometer equipped with an EN4118X-MD4 resonator in the temperature range of 5−200 K. The temperature was controlled using an Oxford Instruments CF935 continuous flow cryostat using liquid He. X-band pulse experiments were obtained from echo, the shot repetition time was set at 409.6 ms, and the $\pi/2$ pulse was set to 16 ns for T_m measurements and 24 ns for inversion magnetization experiments. All EPR measurements were carried out under dark conditions.

Q-band pulsed EPR measurements were carried out at 100 K on a Bruker Elexsys E580 spectrometer operating at 35 GHz and outfitted with a Q-band resonator (EN-5107-D2). The temperature was controlled using an Oxford Instruments CF935 continuous flow cryostat using liquid He. Field-sweep echo-detected (FSED) EPR spectra were recorded using the two-pulse echo sequence ($\pi/2-\tau-\pi-\tau-echo$) where the echo intensity is measured as a function of the magnetic field. The microwave pulse lengths, $\pi/2$ and π, were 14 and 28 ns, respectively, and the time interval between the pulses, τ, was 200 ns. ^{1}H ENDOR spectra were recorded using the Davies ENDOR pulse sequence, $\pi-T-\pi/2-\tau-\pi-\tau-echo$, with the radiofrequency (RF) pulse, applied during the time interval T.

The experimental conditions were t MW 200, 100, 200 ns, τ 400 ns, and the RF pulse length was 18 μs.

The W-band (94 GHz) EPR measurements were conducted on a homebuilt spectrometer described here.[33]

RESULTS AND DISCUSSION

PDA is formed by radical polymerization, forming stable radicals in this process. Beyond this, it also has radical scavenging properties—it is a scavenger of carbon-centered radicals,[34−39] and under ultraviolet light, it can generate hydroxyl free radicals.[40] The mass of PDA, which quenches 50% of 2,2-diphenyl-1-picrylhydrazyl's (DPPH's) EPR signal (ED_{50}), is equal to ~150 μg/3 mL DPPH (100 μM, corresponds to 118.3 μg of DPPH) as previously reported.[39] It was shown that radical scavenging activity increases with the decrease of the nanoparticle's size reaching 68 nm, the values of which are similar to those of ascorbic acid.[37]

From the literature, it is known that at the X-band, single natural melanin exhibits a slightly asymmetrical line[41,42] (line width 4−8 G) sensitive to various conditions such as moisture and oxygenation,[42−44] with the g-factor of the order of ~2.003, and the number of spins is usually in the range of 10^{14} to 10^{17} spins/g.[45] Due to the relatively narrow line, it is possible to apply this radical as an imaging marker in EPR imaging.[46,47] The integral intensity of melanin follows the Curie−Weiss law in a broad temperature range.[41] In all the above-mentioned articles, g-factors are in the range of 2.003−2.0060. The spin−lattice relaxation time T_1 is in the range of 6−100 μs in the temperature range of 4−500 K (20 μs at room temperature). These data were obtained using the CW saturation technique,[41,48,49] which is less accurate than pulse measurements, which will be presented here. Pulse-EPR measurements performed by Ozanaki et al. at a single temperature of 77 K on synthetic melanin showed two spin−lattice relaxation times of 0.1 and 4.3 ms and a spin memory time T_m of 1 μs.[50] Recently appeared pulsed EPR studies of dopa melanin report two spin−lattice relaxation times T_1 for two radical species of 11.5 and 67.9 ms (20 K), which decrease to 0.97 μs and 2.66 ms (110 K), respectively.[51]

Our PDA sample was prepared according to the standard protocol using the oxidative polymerization of dopamine under basic conditions (details in the Experimental Section). The process was not controlled and resulted in a high order of randomness. This led to particle formation in different sizes and ill-defined polymer formation. The morphology of the obtained materials was visualized by SEM (Figure 1a,b). The micrograph in Figure 1a,b shows partially spherical nanoparticles having on average 320 ± 89 nm of PDA agglomerated into larger >100 μm pieces (chunks).

The FTIR spectrum of PDA obtained in the Tris buffer (Figure 1c) shows signals in the range of 1500−1600 cm^{-1} that were assigned to the N−H vibrations. The broad peak spanning 3200−3500 cm^{-1} visible in the spectrum is due to the presence of hydroxyl groups as well as water. Unfortunately, the clear structure of PDA remains unknown, so we could not solve all peaks and identify them unambiguously. Nevertheless, the obtained spectrum is in agreement with previously reported data.[25] The zeta potential of PDA obtained in water was in agreement with the previous report and was close to −30 mV (Figure 1d).

Since the PDA structure is still elusive, it is impossible to predict its real electronic structure (Figure 2). However, there is a consensus in the literature that PDA and related melanin
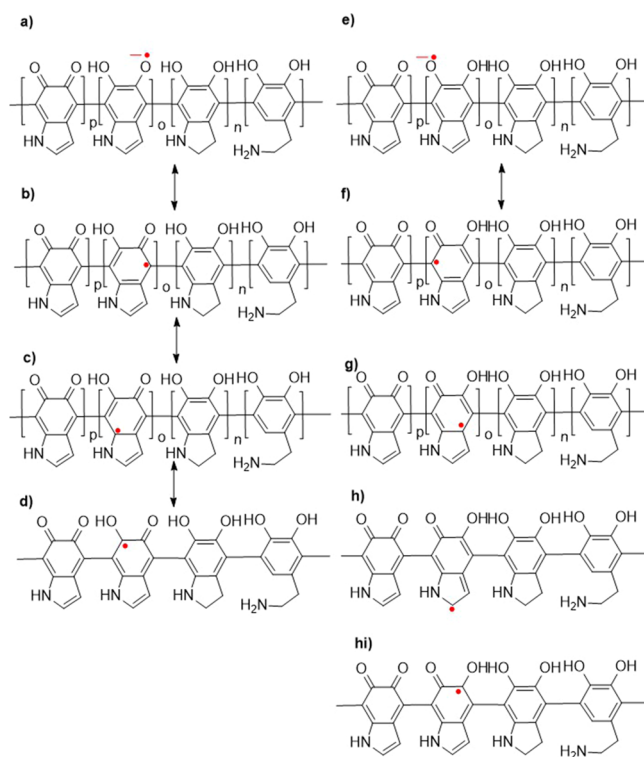

Figure 2. Theoretically predicted resonance structures of PDA radicals.

consist of two distinguished radicals. One of them is a semiquinone type where the radical is localized on the oxygen atom. The second radical is located in the benzene ring of 5,6-dihydroxyindole building PDA and melanins.[29−32] Furthermore, it can be specified that the spin density of this radical has a low density over the nitrogen atom because of the lack of hyperfine splitting from this nucleus in the EPR spectrum (Figure 2). Radicals only show one signal, which is a superposition of two lines with g-factors equal to ~2.003 at the X-band, which makes them indistinguishable without saturating one of these lines with large microwave power while sweeping the magnetic field. The line belonging to the slower relaxing entity with means characterized by a larger T_1 relaxation time will broaden and vanish in the background, while the fast relaxing component will remain almost unchanged if only the difference between their relaxation times is large.[29−32]

Initially, we started with CW-EPR (X-band) measurements on the PDA sample having 15 % wt of moisture. It is worth highlighting that all presented EPR results were obtained under dark conditions since different results for EPR[40] and conductivity were reported depending on dark or light conditions.[52]

The CW-EPR experiment held at the X-band shows a slightly asymmetrical EPR line, which can be simulated by a single Lorentz line with small g-tensor anisotropy, as is shown in Figure 3a. The CW-EPR spectrum recorded at 9 GHz can be simulated well with only one Lorentz line instead of two to obtain a fine fitting fidelity. This shows a strong overlapping of two contributions at this frequency. The following fitting parameters were used: $g_x = g_y = 2.0038$ and $g_z = 2.00125$ with peak-to-peak line widths $\Delta B_{x,y} = 0.4$ mT and $\Delta B_z = 0.485$ mT (EasySpin[53−55]). The normalized integral intensity increases with a decrease of temperature but less than expected for
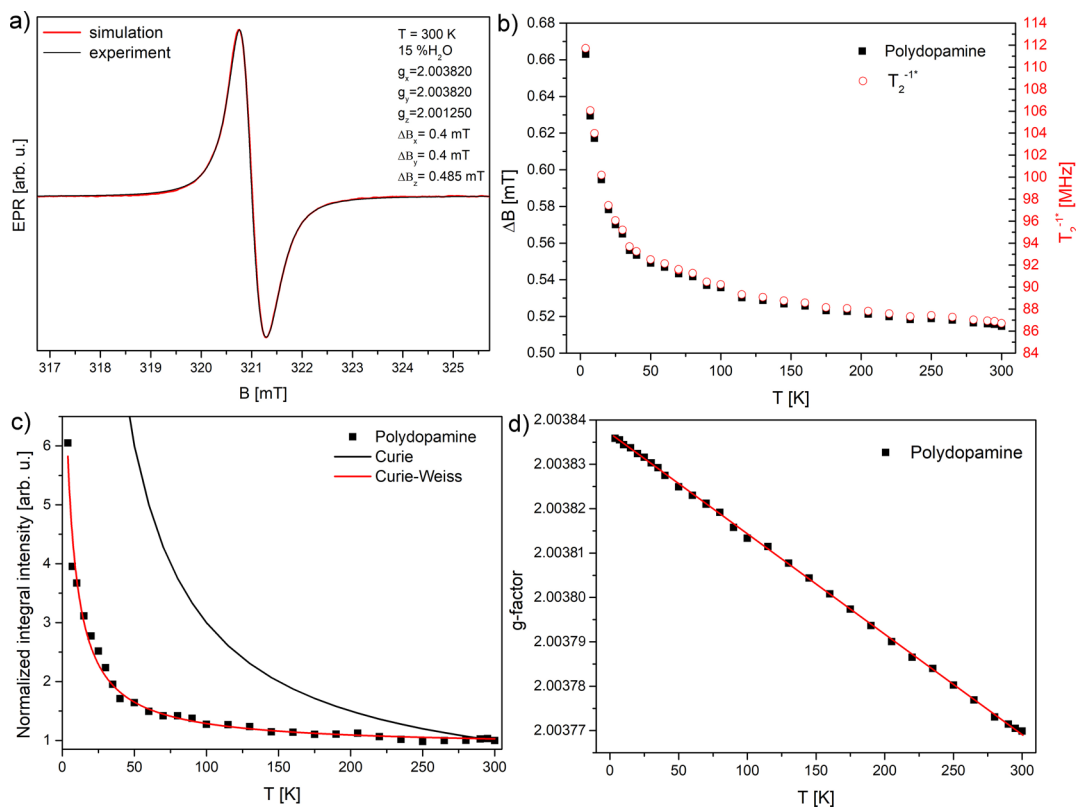
Figure 3. (a) EPR signal recorded at 300 K fitted with the Lorentz line (EasySpin); (b) line width peak-to-peak ΔB_{pp} with a spin–spin relaxation rate estimated with the Bloch relation for homogeneously broadened lines;[58] (c) temperature dependence of the integral intensity with fits Curie and Curie–Weiss functions; (d) temperature dependence of g-factor.

noninteracting localized paramagnetic centers described by the Curie function with the relation $\sim T^{-1}$ (1 at 300 K and 60 at 5 K), which suggests that the delocalization over aromatic ring π-electrons and localized radicals coexist in this system (Figure 3c). Magnetic susceptibility can be described by the Curie–Weiss function $\chi = \frac{C}{T - T_c}$, where $C = 41.6 \pm 2.8$ and $T_c = -4.63 \pm 0.63$ ($R^2 = 0.9868$, Figure 3c), and is similar to the results reported by Skrzypek,[56] which was explained by semiconductor properties and trapping of charge carriers. Gonçalves et al. showed that heating above 60 °C (48 h) decreases the conductivity by 3 orders of magnitude and increases the spin density by a factor of 3, which is a reversible process.[57] Thermal treatments induce the trapping of free protons in carboxylic groups, leading to an increase of the EPR signal and a decrease of conductivity.[57]

The recorded g-factor of PDA (taken in the middle of the cumulative line) increases with the decrease of temperature slightly from 2.0037 to 2.0038 (Figure 3d). The results are in agreement with the results presented in the earlier work.[47] The line width increases with a decrease in temperature, which also implies the increase of T_2^{-1*} relaxation rate (Figure 3b). If applying the Bloch equation for the T_2 time from the EPR line width recorded by CW-EPR, $T_2[s] = \frac{2}{\sqrt{3} \cdot \gamma \cdot \Delta B_{pp}} = \frac{1.3131 \times 10^{-7}}{g \cdot \Delta B_{pp}[G]}$, where ΔB_{pp} is the peak-to-peak line width and g is the Landé factor.[58] The reversed value T_2^{-1*} is called the relaxation rate and is presented in Figure 3b. This value is in fair agreement with directly measured T_2^{-1*} with pulse methods (Figure 5d), although it should be mentioned that the applicability of the Bloch equation is limited to homogeneously broadened lines,

which is not the case here. The values of relaxation rate T_2^{-1*} obtained from CW-EPR are in the range of 112–87 MHz for 4.2–300 K (87.8 MHz at 200 K), and exactly the same values from pulse experiments are in the range of 52–43.6 MHz in the temperature range of 4.2–200 K (Table 2, Figure 5d). The temperature trend of T_2^{-1*} is qualitatively the same in both cases, but quantitatively, the correct values measured directly are ∼46% smaller than those obtained from the line width in CW experiments.

Nevertheless, the analysis performed only with the use of CW methods at a relatively low frequency was not enough to distinguish components of the PDA line. An increase of the spectral resolution in comparison with CW-EPR results presented before can be obtained using pulse techniques even at the X-band. We have performed the FSED experiment. In this experiment, the signal source is the echo intensity obtained after two pulses, while the magnetic field is swept in a selected range (Figure 4a). The result of the field-swept echo-detected experiment gives a single signal, which can be decomposed into two components (Table 1). The lines were approximated using two Gaussian line shapes (fidelity $R^2 = 0.998$). The estimated number of radicals in the PDA sample was found to be 5.5×10^{18} spins/g (from CW-EPR, X-band), which is close to previously reported values.[59,60] Two components appear roughly in the ratio of 1:2 for each case. For results of the same experiment held at the Q-band, it is 10.7/5.3 = 2.0, and at the W-band, it is 1.9, which corresponds to the spin number ratio of ($\sim$3.6/1.9) $\times 10^{18}$ spins/g. The third broad component visible in the W-band with $g \leq 2$ is probably metal contamination coming from the tube (Figure 4b). It is visible only in this setup and does not belong to the
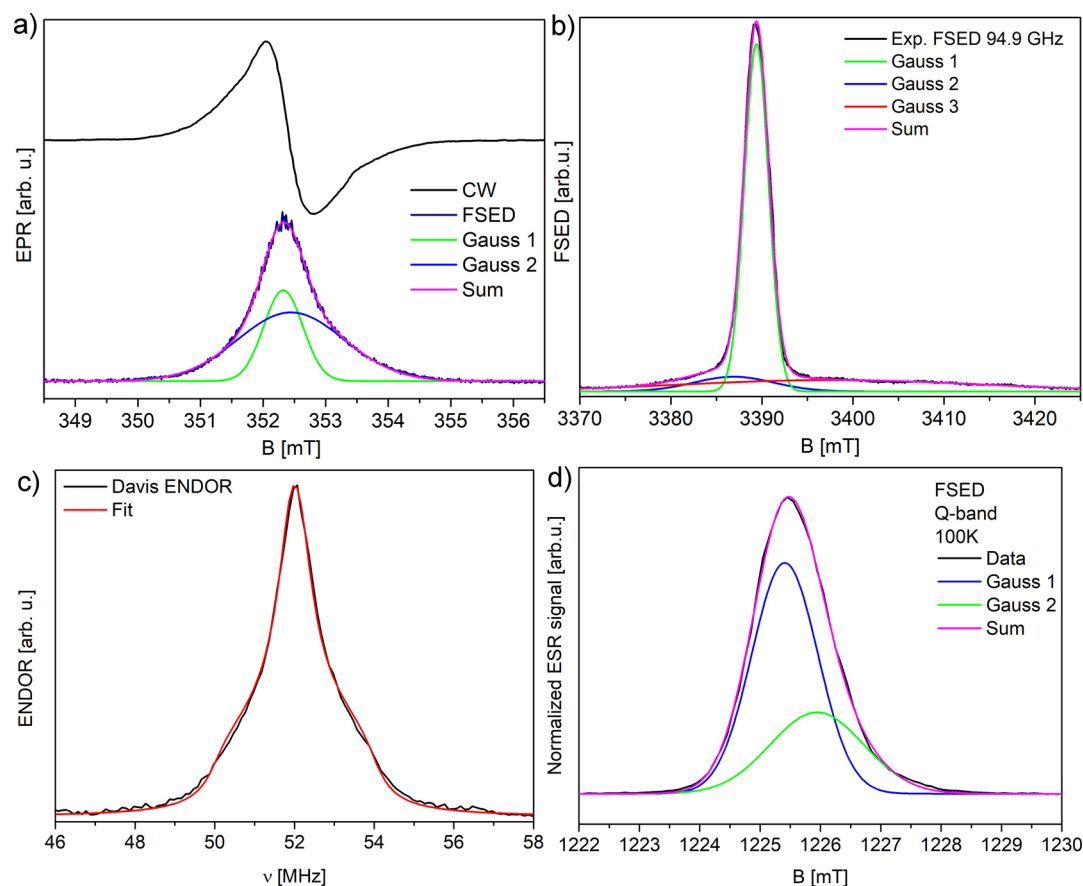
Figure 4. (a) CW (CW-EPR, X-band), field-swept echo-detected spectrum (X-band) and its decomposition in two Gauss line components; (b) W-band spectrum and its decomposition into three Gauss lines; (c) Davis ENDOR ^1H spectrum (Q-band, 100 K); (d) FSED EPR signal at the Q-band (100 K).

Table 1. Parameters of Gauss Components of the PDA Line from the FSED Experiment in Figure 4[a]

band frequency	X-band 9.8 GHz		W-band 94.9 GHz		
line parameters	Gauss 1	Gauss 2	Gauss 1	Gauss 2	Gauss 3
g-factor	2.0037	2.0029	2.0052	2.0037	1.9988
line width [G]	6.2	17.0	10.3	3.1	39.0
A [arb. u.]	4.1	8.5	3.2	22.9	9.4
intensity [arb. u.]	9.1	4.7	10.1	29.8	15.9

[a]The error of g-factors is within ±0.0002 and others within ±0.1.

PDA system (Table 1). The intensity ratio of all three components is 3:1.6:1. If the first two are taken under consideration, the ratio becomes ∼1.9:1, which is similar to the one obtained from X and Q-band measurements. The ^1H Davis electron nuclear double resonance (ENDOR) experiment (Figure 4c, Q-band, 100 K) shows the anisotropic hydrogen spectrum with its fit (EasySpin "salt") with hyperfine anisotropies of $A_{\parallel} = -0.41$ MHz and $A_{\perp} = -4.54$ MHz (axial symmetry assumption) and the Voigth profile with Gauss/Lorentz components of 0.13/0.86 MHz, respectively. Using the equation $A_{\perp} = A_{iso} - T_{\perp}$ and $A_{\parallel} = A_{iso} + 2T_{\perp}$, we obtain $A_{iso} = 1.24$ MHz and $T_{\perp} = 1.65$ MHz. If the point-dipole approximation using the equation $T_{\perp} = g_e g_n \mu_e \mu_n / h r^3$, where $g_{e,n}$ are the electron and nuclear Landé factors, $\mu_{e,n}$ are the electron and nuclear magnetons, h is the Planck constant, and r is the distance between the electron radical and hydrogen nucleus in this case, is applied, the distance between the radical and the closest hydrogen atom r is 0.37 nm.[61]

Electron Spin Relaxation. The data were evaluated as follows: the spin−lattice relaxation time was obtained with the following equation: $V(t) = M\left(1 - \left(1 - \frac{M_1}{M}\right) \times \exp\left(-\frac{t}{T_1}\right)\right)$ (for each component), which takes under consideration partial inversion of magnetization M_1/M (from echo intensity). The spin−spin relaxation time T_2^* was obtained with the equation $V(t) = M \times \left(\exp\left(-\frac{t}{T_2^*}\right)\right)$, where M is the amplitude of an echo. The phase memory time T_m was obtained with the equation $V(2\tau) = M \times \exp\left(-\frac{2\tau}{T_m}\right)$, where M is the echo intensity as a function of dwell time τ between pulses (Figure 5).

Two spin−lattice relaxation times were obtained and depicted as T_{1A} and T_{1B} (Figure 5b,c). The largest difference in values is observed at the lowest temperature of 5 K, which is 2.14 ms ($T_{1A}^{-1} = 0.47$ kHz) and 46.9 ms ($T_{1B}^{-1} = 0.021$ kHz, Table 2). This suggests the existence of two different species where one is strongly coupled to the lattice for which local phonons efficiently dissipate microwave energy, characterized by T_{1A}, and the second is weakly coupled to the lattice, characterized by a much longer time T_{1B}. If comparing PDA with previously studied carbon-ring based systems, such as graphene oxide (rich in oxygen groups) similarly long T_1 time
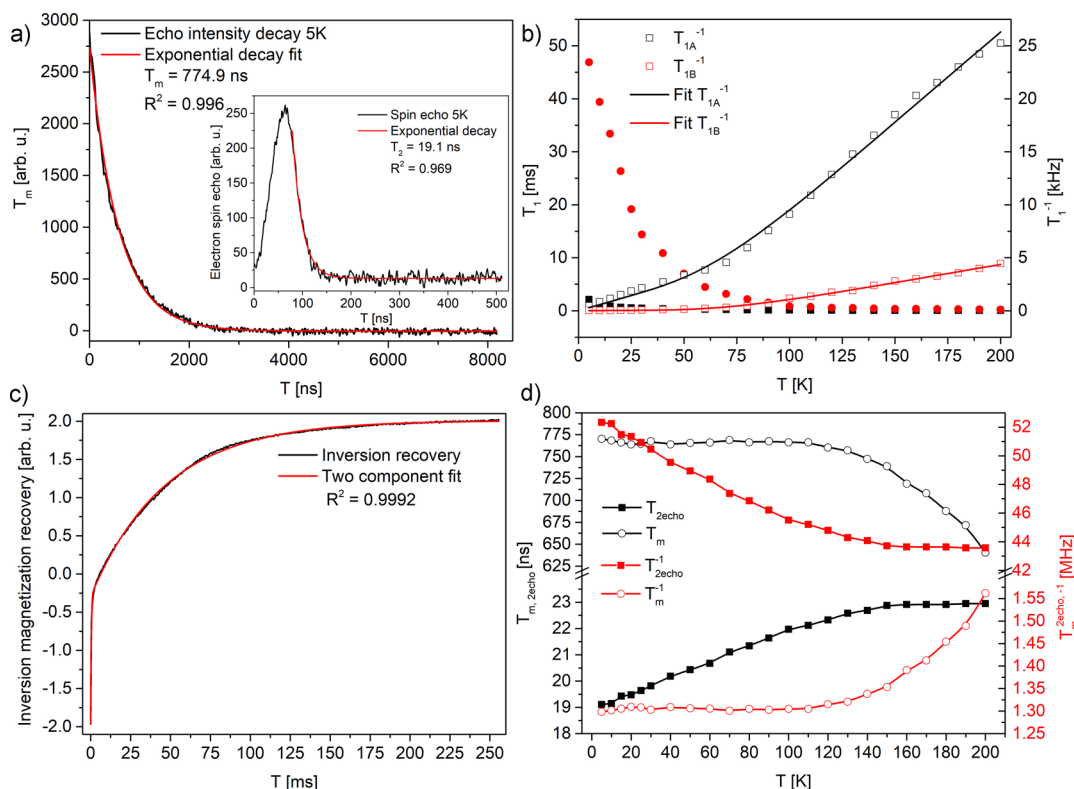
Figure 5. (a) Phase memory time decay in 5 K; (inset) spin-echo and T_2 decay vs time (from echo); (b) temperature dependences of spin−lattice $T_{1A,B}$ components and the rates with TLS model fits; (c) inversion recovery of an echo, recorded at 5 K; (d) temperature dependences of T_2 and T_m and the relaxation rates.

Table 2. Electron Spin Relaxation Times and Rates[a]

temperature [K]	T_{1A} [ms] (T_{1A}^{-1} [kHz])	T_{1B} [ms] (T_{1B}^{-1} [kHz])	T_m [ns] (T_m^{-1} [MHz])	T_2^* [ns] (T_2^{*-1} [MHz])
5	2.14 (0.47)	46.9 (0.021)	770 (1.3)	19.1 (52.33)
200	0.0396 (25.24)	0.224 (4.46)	640 (1.56)	22.95 (43.57)

[a]Errors within: $T_{1A,B}$ ±5 ms, T_m ±50 ns, T_2^* ±5 ns.

was measured. Signal belongs to oxygen species located outside the graphene ring.[62−64] After reduction, much shorter relaxation times were observed. Probably, the radical with a longer relaxation time is also separated from the carbon ring and located on an oxygen group. If the PDA system is compared to other disordered, solid, carbon-based samples, the relaxation can be considered as slow. Relaxation rates in PDA are 2.5 and 10 kHz at 100 K. In graphene-based materials, it is, e.g. in graphene nanoribbons T_1^{-1} ~14 kHz and 100 kHz,[65] in graphene $T_1^{-1} \sim T_2^{-1*} \sim$ 3 MHz,[66] in partially reduced graphene oxide 17.5 MHz[67] in graphene oxide it is ~1 kHz.[63] In all these systems, reduction, which causes an increase in conductivity and larger delocalization of electrons over carbon rings, decreases the spin−lattice relaxation time. This makes it more probable in the PDA system that a long relaxation time is likely to be found on oxygen groups further from the carbon ring like it was found for graphene oxide.[63]

The spin−lattice relaxation process can be described by tunneling of two-level systems (TLSs)—the TLS model which described soft local oscillators, localized phonons. This model can be used for describing electron relaxation of amorphous disordered solid systems, for example, polymers.[65,68,69] The temperature dependence of the spin−lattice relaxation rate in

the TLS model can be described[69] in the form $1/T_{1A} = A \times T + B \times \mathrm{Cosh}(\Delta/kT)$, with fitting parameters as follows: $A = (57.2 \pm 6.4) \times 10^{-6}$ K^{-1} s^{-1}, $B = (25.0 \pm 2.6) \times 10^{-3}$, and $\Delta = 258.9 \pm 25.7$ K, $R^2 = 0.9987$, and for the second process $(1/T_{1B})$ with parameters as follows: $A = (1.2 \pm 0.9) \times 10^{-6}$ K^{-1} s^{-1}, $B = (8.0 \pm 0.5) \times 10^{-3}$, and $\Delta = 284.8 \pm 14.8$ K, $R^2 = 0.9987$. The linear relaxation process dominates up to 50 K. Such dependence can be produced by various mechanisms, such as modulations of the hyperfine coupling by tunneling TLS at low temperatures, modulations of the singlet−triplet splitting of exchange coupled pairs by local dynamics, and/or local oscillator dynamics. At higher temperatures, excitations with energy Δ are the dominating relaxation mechanisms.[69,70]

The phase memory time T_m is constant below 100 K, but at higher temperatures, it starts to decrease, which is connected with the broadening of spin packets under the inhomogeneously broadened line (Figure 5a,d, Table 2). This broadening can be attributed to the thermal activation of the local dynamics of −OH and −NH$_2$ groups, which, above 200 K, could lead to a minimum of T_m when the spin packet frequencies will average (above the measured temperature range). In connection with the increase of T_2 time, which is responsible for the observable line width ΔB, the signal broadening homogenizes probably due to spin diffusion processes. The increase of T_2^{-1} relaxation rate with a decrease of temperature corresponds qualitatively with the increase of the line width ΔB from CW measurements.

■ CONCLUSIONS

The new approach toward EPR studies of PDA using pulse X-band (9 GHz), Q-band (34 GHz), and W-band (94.4 GHz) FSED and relaxation measurements confirmed the presence of

two radical species in a quantitative ratio of ∼1:2. The increase of spectral resolution when changing from the X-band to W-band was not enough to clearly separate the components of the EPR signal, but fitting showed two components with different g-factors under one unresolved line. Both radical species show different temperature relaxation behaviors, which suggest different spatial coordinates. A lack of visible hyperfine splitting suggests a low radical spin density over the nitrogen nucleus. Under the assumption of axial anisotropy and point-dipole approximation, the shortest distance r between one of the radicals and the hydrogen atom is 0.37 nm. By comparison with other carbon-ring systems, it is assumed that the semiquinone (oxygen-based) radical exhibits a longer relaxation time of T_1 = 46.9 ms at 5 K (T_1^{-1} = 21 Hz) than the radical delocalized on the carbon ring. The temperature dependence of the spin−lattice relaxation rate T_1^{-1} could be well approximated with the TLS model, which was previously applied for amorphous and disordered solid systems.

The data that support the findings of this study are available from the corresponding author upon reasonable request.

■ AUTHOR INFORMATION

Corresponding Author

Krzysztof Tadyszak − *Institute of Molecular Physics, Polish Academy of Sciences, 60-179 Poznan, Poland; Institute of Chemistry and Biochemistry, Free University of Berlin, 14195 Berlin, Germany;* ● orcid.org/0000-0002-0370-9766; Email: krzysztof.tadyszak@ifmpan.poznan.pl

Authors

Radosław Mrówczyński − *NanoBioMedical Centre and Department of Chemistry, Adam Mickiewicz University, 61-614 Poznan, Poland;* ● orcid.org/0000-0003-3687-911X

Raanan Carmieli − *Department of Chemical Research Support Faculty of Chemistry, Weizmann Institute of Science, 76100 Rehovot, Israel;* ● orcid.org/0000-0003-4418-916X

Complete contact information is available at:
https://pubs.acs.org/10.1021/acs.jpcb.0c10485

Notes

The authors declare no competing financial interest.

■ ACKNOWLEDGMENTS

■ REFERENCES

(1) Shalev, T.; Gopin, A.; Bauer, M.; Stark, R. W.; Rahimipour, S. Non-leaching antimicrobial surfaces through polydopamine bio-inspired coating of quaternary ammonium salts or an ultrashort antimicrobial lipopeptide. *J. Mater. Chem.* **2012**, *22*, 2026−2032.

(2) Tsai, W.-B.; Chen, W.-T.; Chien, H.-W.; Kuo, W.-H.; Wang, M.-J. Poly(dopamine) coating of scaffolds for articular cartilage tissue engineering. *Acta Biomater.* **2011**, *7*, 4187−4194.

(3) Kim, J. H.; Lee, M.; Park, C. B. Polydopamine as a Biomimetic Electron Gate for Artificial Photosynthesis. *Angew. Chem., Int. Ed.* **2014**, *53*, 6364−6368.

(4) Mrówczyński, R.; Bunge, A.; Liebscher, J. Polydopamine-An Organocatalyst Rather than an Innocent Polymer. *Chem.—Eur. J.* **2014**, *20*, 8647−8653.

(5) Kim, Y.; Coy, E.; Kim, H.; Mrówczyński, R.; Torruella, P.; Jeong, D.-W.; Choi, K. S.; Jang, J. H.; Song, M. Y.; Jang, D.-J.; Peiro, F.; Jurga, S.; Kim, H. J. Efficient photocatalytic production of hydrogen by exploiting the polydopamine-semiconductor interface. *Appl. Catal., B* **2020**, *280*, 119423.

(6) Fedorenko, V.; Viter, R.; Mrówczyński, R.; Damberga, D.; Coy, E.; Iatsunskyi, I. Synthesis and photoluminescence properties of hybrid 1D core-shell structured nanocomposites based on ZnO/polydopamine. *RSC Adv.* **2020**, *10*, 29751−29758.

(7) Cui, J.; Yan, Y.; Such, G. K.; Liang, K.; Ochs, C. J.; Postma, A.; Caruso, F. Immobilization and Intracellular Delivery of an Anticancer Drug Using Mussel-Inspired Polydopamine Capsules. *Biomacromolecules* **2012**, *13*, 2225−2228.

(8) Liu, Y.; Ai, K.; Lu, L. Polydopamine and Its Derivative Materials: Synthesis and Promising Applications in Energy, Environmental, and Biomedical Fields. *Chem. Rev.* **2014**, *114*, 5057−5115.

(9) Lynge, M. E.; van der Westen, R.; Postma, A.; Städler, B. Polydopamine-a nature-inspired polymer coating for biomedical science. *Nanoscale* **2011**, *3*, 4916−4928.

(10) Shin, Y. M.; Lee, Y. B.; Kim, S. J.; Kang, J. K.; Park, J.-C.; Jang, W.; Shin, H. Mussel-Inspired Immobilization of Vascular Endothelial Growth Factor (VEGF) for Enhanced Endothelialization of Vascular Grafts. *Biomacromolecules* **2012**, *13*, 2020−2028.

(11) Ren, Y.; Rivera, J. G.; He, L.; Kulkarni, H.; Lee, D.-K.; Messersmith, P. Facile, high efficiency immobilization of lipase enzyme on magnetic iron oxide nanoparticles via a biomimetic coating. *BMC Biotechnol.* **2011**, *11*, 63.

(12) Gao, X.; Ni, K.; Zhao, C.; Ren, Y.; Wei, D. Enhancement of the activity of enzyme immobilized on polydopamine-coated iron oxide nanoparticles by rational orientation of formate dehydrogenase. *J. Biotechnol.* **2014**, *188*, 36−41.

(13) Lee, H.; Rho, J.; Messersmith, P. B. Facile Conjugation of Biomolecules onto Surfaces via Mussel Adhesive Protein Inspired Coatings. *Adv. Mater.* **2009**, *21*, 431−434.

(14) Mrówczyński, R.; Turcu, R.; Leostean, C.; Scheidt, H. A.; Liebscher, J. New versatile polydopamine coated functionalized magnetic nanoparticles. *Mater. Chem. Phys.* **2013**, *138*, 295−302.

(15) Cont, L.; Grant, D.; Scotchford, C.; Todea, M.; Popa, C. Composite PLA scaffolds reinforced with PDO fibers for tissue engineering. *J. Biomater. Appl.* **2013**, *27*, 707−716.

(16) Luo, R.; Tang, L.; Wang, J.; Zhao, Y.; Tu, Q.; Weng, Y.; Shen, R.; Huang, N. Improved immobilization of biomolecules to quinone-rich polydopamine for efficient surface functionalization. *Colloids Surf., B* **2013**, *106*, 66−73.

(17) Lee, H.; Lee, B. P.; Messersmith, P. B. A reversible wet/dry adhesive inspired by mussels and geckos. *Nature* **2007**, *448*, 338−341.

(18) Martín, M.; Salazar, P.; Villalonga, R.; Campuzano, S.; Pingarrón, J. M.; González-Mora, J. L. Preparation of core-shell Fe3O4@poly(dopamine) magnetic nanoparticles for biosensor construction. *J. Mater. Chem. B* **2014**, *2*, 739−746.

(19) Mrówczyński, R.; Jurga-Stopa, J.; Markiewicz, R.; Coy, E. L.; Jurga, S.; Woźniak, A. Assessment of polydopamine coated magnetic nanoparticles in doxorubicin delivery. *RSC Adv.* **2016**, *6*, 5936−5943.

(20) Mrówczyński, R.; Jędrzak, A.; Szutkowski, K.; Grześkowiak, B. F.; Coy, E.; Markiewicz, R.; Jesionowski, T.; Jurga, S. Cyclodextrin-Based Magnetic Nanoparticles for Cancer Therapy. *Nanomaterials* **2018**, *8*, 170.

(21) Petran, A.; Mrówczyński, R.; Filip, C.; Turcu, R.; Liebscher, J. Melanin-like polydopa amides - synthesis and application in functionalization of magnetic nanoparticles. *Polym. Chem.* **2015**, *6*, 2139−2149.

(22) Jędrzak, A.; Grześkowiak, B. F.; Coy, E.; Wojnarowicz, J.; Szutkowski, K.; Jurga, S.; Jesionowski, T.; Mrówczyński, R. Dendrimer based theranostic nanostructures for combined chemo- and photo-thermal therapy of liver cancer cells in vitro. *Colloids Surf., B* **2019**, *173*, 698−708.

(23) Jędrzak, A.; Rębiś, T.; Nowicki, M.; Synoradzki, K.; Mrówczyński, R.; Jesionowski, T. Polydopamine grafted on an advanced Fe3O4/lignin hybrid material and its evaluation in biosensing. *Appl. Surf. Sci.* **2018**, *455*, 455−464.

(24) Longuet-Higgins, H. C. On the origin of the free radical property of melanins. *Arch. Biochem. Biophys.* **1960**, *86*, 231−232.

(25) Liebscher, J.; Mrówczyński, R.; Scheidt, H. A.; Filip, C.; Hădade, N. D.; Turcu, R.; Bende, A.; Beck, S. Structure of Polydopamine: A Never-Ending Story? *Langmuir* **2013**, *29*, 10539−10548.

(26) Yu, X.; Fan, H.; Liu, Y.; Shi, Z.; Jin, Z. Characterization of Carbonized Polydopamine Nanoparticles Suggests Ordered Supramolecular Structure of Polydopamine. *Langmuir* **2014**, *30*, 5497−5505.

(27) Dreyer, D. R.; Miller, D. J.; Freeman, B. D.; Paul, D. R.; Bielawski, C. W. Elucidating the Structure of Poly(dopamine). *Langmuir* **2012**, *28*, 6428−6435.

(28) Tran, M. L.; Powell, B. J.; Meredith, P. Chemical and Structural Disorder in Eumelanins: A Possible Explanation for Broadband Absorbance. *Biophys. J.* **2006**, *90*, 743−752.

(29) Della Vecchia, N. F.; Luchini, A.; Napolitano, A.; D'Errico, G.; Vitiello, G.; Szekely, N.; d'Ischia, M.; Paduano, L. Tris Buffer Modulates Polydopamine Growth, Aggregation, and Paramagnetic Properties. *Langmuir* **2014**, *30*, 9811−9818.

(30) Mostert, A. B.; Hanson, G. R.; Sarna, T.; Gentle, I. R.; Powell, B. J.; Meredith, P. Hydration-Controlled X-Band EPR Spectroscopy: A Tool for Unravelling the Complexities of the Solid-State Free Radical in Eumelanin. *J. Phys. Chem. B* **2013**, *117*, 4965−4972.

(31) Mostert, A. B.; Rienecker, S. B.; Noble, C.; Hanson, G. R.; Meredith, P. The photoreactive free radical in eumelanin. *Sci. Adv.* **2018**, *4*, No. eaaq1293.

(32) Sarna, T.; Plonka, P. M. Biophysical Studies of Melanin. In *Biomedical EPR, Part A: Free Radicals, Metals, Medicine, and Physiology*; Eaton, S. R., Eaton, G. R., Berliner, L. J., Eds; Springer: Boston, MA, 2005; Vol. *23*.

(33) Goldfarb, D.; Lipkin, Y.; Potapov, A.; Gorodetsky, Y.; Epel, B.; Raitsimring, A. M.; Radoul, M.; Kaminker, I. HYSCORE and DEER with an upgraded 95GHz pulse EPR spectrometer. *J. Magn. Reson.* **2008**, *194*, 8−15.

(34) Sarna, T.; Pilas, B.; Land, E. J.; Truscott, T. G. Interaction of radicals from water radiolysis with melanin. *Biochim. Biophys. Acta Gen. Subj.* **1986**, *883*, 162−167.

(35) Dunford, R.; Land, E. J.; Rozanowska, M.; Sarna, T.; Truscott, T. G. Interaction of melanin with carbon- and oxygen-centered radicals from methanol and ethanol. *Free Radic. Biol. Med.* **1995**, *19*, 735−740.

(36) Blarzino, C.; Mosca, L.; Foppoli, C.; Coccia, R.; De Marco, C.; Rosei, M. A. Lipoxygenase/H2O2-catalyzed oxidation of dihydroxyindoles: synthesis of melanin pigments and study of their antioxidant properties. *Free Radic. Biol. Med.* **1999**, *26*, 446−453.

(37) Ju, K.-Y.; Lee, Y.; Lee, S.; Park, S. B.; Lee, J.-K. Bioinspired Polymerization of Dopamine to Generate Melanin-Like Nanoparticles Having an Excellent Free-Radical-Scavenging Property. *Biomacromolecules* **2011**, *12*, 625−632.

(38) Liu, Y.; Ai, K.; Ji, X.; Askhatova, D.; Du, R.; Lu, L.; Shi, J. Comprehensive Insights into the Multi-Antioxidative Mechanisms of Melanin Nanoparticles and Their Application To Protect Brain from Injury in Ischemic Stroke. *J. Am. Chem. Soc.* **2017**, *139*, 856−862.

(39) Liu, H.; Qu, X.; Tan, H.; Song, J.; Lei, M.; Kim, E.; Payne, G. F.; Liu, C. Role of polydopamine's redox-activity on its pro-oxidant, radical-scavenging, and antimicrobial activities. *Acta Biomater.* **2019**, *88*, 181−196.

(40) Wang, Z.; Tang, F.; Fan, H.; Wang, L.; Jin, Z. Polydopamine Generates Hydroxyl Free Radicals under Ultraviolet-Light Illumination. *Langmuir* **2017**, *33*, 5938−5946.

(41) Blois, M. S.; Zahlan, A. B.; Maling, J. E. Electron spin resonance studies on melanin. *Biophys. J.* **1964**, *4*, 471−490.

(42) Scaly, R. C.; Felix, C. C.; Hyde, J. S.; Swartz, H. M. Structure and reactivity of melanins: influence of free radicals and metal ions. In

Free Radicals in Biology, Pryor, W. P., Ed.; Academic Press: New York, 1980; Vol. 4, pp 209−259.

(43) Korytowski, W.; Hintz, P.; Sealy, R. C.; Kalyanaraman, B. Mechanism of dismutation of superoxide produced during autoxidation of melanin pigments. *Biochem. Biophys. Res. Commun.* **1985**, *131*, 659−665.

(44) Sarna, T.; Dulęba, A.; Korytowski, W.; Swartz, H. Interaction of melanin with oxygen. *Arch. Biochem. Biophys.* **1980**, *200*, 140−148.

(45) Mason, H. S.; Ingram, D. J. E.; Allen, B. The free radical property of melanins. *Arch. Biochem. Biophys.* **1960**, *86*, 225−230.

(46) Jang, H.; Subramanian, S.; Devasahayam, N.; Saito, K.; Matsumoto, S.; Krishna, M. C.; McMillan, A. B. Single Acquisition Quantitative Single-Point Electron Paramagnetic Resonance Imaging. *Magn. Reson. Med.* **2013**, *70*, 1173−1181.

(47) Mrówczyński, R.; Coy, L. E.; Scheibe, B.; Czechowski, T.; Augustyniak-Jabłokow, M.; Jurga, S.; Tadyszak, K. Electron Paramagnetic Resonance Imaging and Spectroscopy of Polydopamine Radicals. *J. Phys. Chem. B* **2015**, *119*, 10341−10347.

(48) Chodurek, E.; Zdybel, M.; Pilawa, B.; Dzierzewicz, Z. Examination by EPR spectroscopy of free radicals in melanins isolated from A-375 cells exposed on valproic acid and cisplatin. *Acta Pol. Pharm.* **2012**, *69*, 1334−1341.

(49) Chodurek, E.; Zdybel, M.; Pilawa, B. Application of EPR spectroscopy to examination of free radicals in melanins from A-375 and G-361 human melanoma malignum cells. *J. Appl. Biomed.* **2013**, *11*, 173−185.

(50) Okazaki, M.; Kuwata, K.; Miki, Y.; Shiga, S.; Shiga, T. Electron spin relaxation of synthetic melanin and melanin-containing human tissues as studied by electron spin echo and electron spin resonance. *Arch. Biochem. Biophys.* **1985**, *242*, 197−205.

(51) Al Khatib, M.; Costa, J.; Baratto, M. C.; Basosi, R.; Pogni, R. Paramagnetism and Relaxation Dynamics in Melanin Biomaterials. *J. Phys. Chem. B* **2020**, *124*, 2110−2115.

(52) Mostert, A. B.; Powell, B. J.; Gentle, I. R.; Meredith, P. On the origin of electrical conductivity in the bio-electronic material melanin. *Appl. Phys. Lett.* **2012**, *100*, 093701.

(53) Stoll, S.; Schweiger, A. EasySpin, a comprehensive software package for spectral simulation and analysis in EPR. *J. Magn. Reson.* **2006**, *178*, 42−55.

(54) Stoll, S. CW-EPR Spectral Simulations: Solid State. In *Methods in Enzymology*; Qin, P. Z., Warncke, K., Eds.; Academic Press, 2015; Chapter 6, Vol. *563*, pp 121−142.

(55) Stoll, S. Computational Modeling and Least-Squares Fittingof EPR Spectra. *Multifrequency Electron Paramagnetic Resonance*; Wiley, 2014; pp 69−138.

(56) Skrzypek, D.; Dzierżęga-Lęcznar, A.; Ziółkowska, J. EPR Investigations of Model Neuromelanins. *Acta Phys. Pol., A* **2000**, *98*, 561−566.

(57) Gonçalves, P. J.; Filho, O. B.; Graeff, C. F. O. Effects of hydrogen on the electronic properties of synthetic melanin. *J. Appl. Phys.* **2006**, *99*, 104701.

(58) Charles, P.; Pool, J. *Electron Spin resonance A Comprehensive Treatise on Experimental Techniques*; Denver Publications, INC.: Mineola, New York, 1983.

(59) Yordanov, N. D. Quantitative EPR spectrometry — "State of the art". *Appl. Magn. Reson.* **1994**, *6*, 241−257.

(60) Dyrek, K.; Rokosz, A.; Madej, A. Spin dosimetry in catalysis research. *Appl. Magn. Reson.* **1994**, *6*, 309−332.

(61) Schiemann, O.; Carmieli, R.; Goldfarb, D. W-band31P-ENDOR on the high-affinity Mn2+ binding site in the minimal and tertiary stabilized hammerhead ribozymes. *Appl. Magn. Reson.* **2007**, *31*, 543−552.

(62) Augustyniak-Jabłokow, M. A.; Strzelczyk, R.; Fedaruk, R. Localization of conduction electrons in hydrothermally reduced graphene oxide: Electron paramagnetic resonance studies. *Carbon* **2020**, *168*, 665.

(63) Augustyniak-Jabłokow, M. A.; Tadyszak, K.; Strzelczyk, R.; Fedaruk, R.; Carmieli, R. Slow spin relaxation of paramagnetic centers in graphene oxide. *Carbon* **2019**, *152*, 98−105.

(64) Augustyniak-Jabłokow, M. A.; Fedaruk, R.; Strzelczyk, R.; Majchrzycki, Ł. Identification of a Slowly Relaxing Paramagnetic Center in Graphene Oxide. *Appl. Magn. Reson.* **2019**, *50*, 761–768.

(65) Rao, S. S.; Stesmans, A.; van Tol, J.; Kosynkin, D. V.; Higginbotham-Duque, A.; Lu, W.; Sinitskii, A.; Tour, J. M. Spin Dynamics and Relaxation in Graphene Nanoribbons: Electron Spin Resonance Probing. *ACS Nano* **2012**, *6*, 7615–7623.

(66) Augustyniak-Jabłokow, M. A.; Tadyszak, K.; Maćkowiak, M.; Lijewski, S. ESR study of spin relaxation in graphene. *Chem. Phys. Lett.* **2013**, *557*, 118.

(67) Tadyszak, K.; Chybczyńska, K.; Ławniczak, P.; Zalewska, A.; Cieniek, B.; Gonet, M.; Murias, M. Magnetic and electric properties of partially reduced graphene oxide aerogels. *J. Magn. Magn. Mater.* **2019**, *492*, 165656.

(68) Golding, B.; Graebner, G. Relaxation Times of Tunneling Systems in Glasses. In *Amorphous Solids*; Phillips, W. A., Ed.; Topics in Current Physics; Springer: Berlin, Heidelberg, 1981; Vol. *24*, p 899.

(69) Hoffmann, S. K.; Hilczer, W.; Radczyk, T.; Polus, I. Electron Spin-Lattice Relaxation in Polymers and Crystals Related to Disorder and Structure Defects. *Acta Phys. Pol., A* **2003**, *103*, 373–385.

(70) Lijewski, S.; Wencka, M.; Hoffmann, S. K.; Kempinski, M.; Kempinski, W.; Sliwinska-Bartkowiak, M. Electron spin relaxation and quantum localization in carbon nanoparticle: Electron spin echo studies. *Phys. Rev. B: Condens. Matter Mater. Phys.* **2008**, *77*, 014304.